ADVANCED FUNCTIONAL MATERIALS
www.afm-journal.de

2D Germanane-MXene Heterostructures for Cations Intercalation in Energy Storage Applications

*Kalyan Ghosh, Siowwoon Ng, Petr Lazar, Akshay Kumar K. Padinjareveetil, Jan Michalička, and Martin Pumera**

Heterostructures offer an exceptional possibility of combining individual 2D materials into a new material having altered properties compared to the parent materials. Germanane (GeH) is a 2D material with many favorable properties for energy storage and catalysis, however, its performance is hindered by its low electrical conductivity. To address the low electrochemical performance of GeH, a heterostructure of GeH and $Ti_3C_2T_x$ is fabricated. The $Ti_3C_2T_x$ is a layered material belonging to the family of MXenes. The resulting heterostructure (GeMXene) at a defined mass ratio of GeH and $Ti_3C_2T_x$ shows superior capacitive performance that surpasses that of both pristine materials. The effect of the size of cations and anions for intercalation into GeMXene in different aqueous salt solutions is studied. GeMXene allows only cation intercalation, which is evidenced by the gravimetric electrochemical quartz crystal microbalance (EQCM) technique. The capacitive performance of the GeMXene is compared in neutral, acidic, and alkaline electrolytes to determine the best electrochemical performance. This unleashes the potential use of GeMXene heterostructure in different electrolytes for supercapacitors and batteries. This work will pave the way to explore the heterostructures of other 2D materials such as novel MXenes and functionalized germanane for highly energy-storage efficient systems, and beyond.

1. Introduction

With the increasing demand for portable electronics and electric vehicles, there is an increasing demand for high-power and high-energy storage devices.[1,2] To meet the requisite, 2D layered materials have been widely explored in the energy storage field because of their exceptional physical and chemical properties.[3,4] Such materials can accommodate plenty of ions in between two single layers without considerably changing their structure. The intercalation of ions between atomic layers provides high capacitance even at a high discharge rate.[4,5]

To explore the 2D layered materials beyond graphene and transition metal dichalcogenides (TMDs),[6,7] researchers emanated with new 2D layered material, an analog of graphene, germanane (GeH), which is hydrogen terminated 2D allotrope of germanium (Ge).[8] GeH is obtained from the Zintl phase $CaGe_2$ by deintercalation of calcium and possesses unique physical and chemical

---

K. Ghosh, S. Ng, A. K. K. Padinjareveetil, M. Pumera
Future Energy and Innovation Laboratory
Central European Institute of Technology
Brno University of Technology
Purkyňova 123, Brno 61200, Czech Republic
E-mail: martin.pumera@ceitec.vutbr.cz

P. Lazar
Regional Centre of Advanced Technologies and Materials
Czech Advanced Technology and Research Institute (CATRIN)
Palacký University Olomouc
Šlechtitelů 27, Olomouc 77900, Czech Republic

The ORCID identification number(s) for the author(s) of this article can be found under https://doi.org/10.1002/adfm.202308793

DOI: 10.1002/adfm.202308793

J. Michalička
Central European Institute of Technology
Brno University of Technology
Purkyňova 123, Brno 61200, Czech Republic

M. Pumera
Faculty of Electrical Engineering and Computer Science
VSB–Technical University of Ostrava
17. listopadu 2172/15, Ostrava 70800, Czech Republic

M. Pumera
Department of Medical Research
China Medical University Hospital
China Medical University
No. 91 Hsueh-Shih Road, Taichung 40402, Taiwan

M. Pumera
Department of Chemical and Biomolecular Engineering
Yonsei University
50 Yonsei-ro, Seodaemun-gu, Seoul 03722, South Korea

properties.[8,9] The Ge nanoparticles and 2D GeH have emerged as potential candidates for batteries and supercapacitors due to their high intercalation charge-storing capability.[10–12] Ge shows a high theoretical capacity of 1384 mAh g^{-1} and high electron mobility of 3900 cm^2 V^{-1} s^{-1}.[12] The GeH structure can be modified by several alkyl functional groups such as methyl, propyl, and other alkyl groups to fabricate derivatives of germanane and tuning its electrochemical properties.[13–16] However, Ge nano/microparticles and GeH undergo severe volume expansion of ≈230−300% during Li-alloying process that can fracture Ge-based nanomaterials and detach the active materials from the current collector surface. This causes fast capacity fading in the long-run cyclic charge–discharge processes.[11,12,17] To prevent this issue, Ge-based nanomaterials are combined with other carbon-based materials such as amorphous carbon,[18,19] carbon nanotubes,[20,21] graphene,[22,23] polypyrrole,[24] that serve as the base matrix providing lower volume expansion and greater cyclic stability.[20]

Alternatively, recently discovered outstanding 2D materials called MXenes, which are 2D transition metal carbides, nitrides, and carbonitrides, have been found to be promising for energy storage applications because of their high mechanical strength, metallic conductivity (≈8700 S cm^{-1}),[25] tunable interlayer distance, and pseudocapacitive and intercalative charge storing capability.[26,27] Among the MXenes family, $Ti_3C_2T_x$ (“T” stands for a surface terminating group such as —F, —OH, and —O) has been widely explored for use in materials for Li-ion batteries and Li-ion capacitors.[27–30] Lukatskaya et al. demonstrated spontaneous intercalation of cations from aqueous solutions into $Ti_3C_2T_x$ layers.[5] It was surmised that the intercalation of ions in $Ti_3C_2T_x$ was affected by the surface termination “T” group. The theoretical gravimetric capacity of the $Ti_3C_2T_x$ for bare, O-terminated, F-terminated, and OH-terminated have been calculated to be 320, 268, 130, and 67 mAh g^{-1}, respectively.[31] The surface termination group controls the intercalation of various types of ions (cations or anions).[32] However, the van der Waals interactions among the 2D layers of $Ti_3C_2T_x$ cause restacking of sheets and hindrance of transport of electrolyte ions inside 2D layers.[33,34]

2D heterostructures create unique possibilities through the stacking of 2D layered materials such as graphene, TMDs, boron nitrides, MXenes, and germanium.[35–39] The heterostructures provide properties additional to those of the pristine 2D materials due to synergistic effects. The heterostructures of TMDs/MXenes,[39,40] TMDs/graphene,[41,42] MXene/graphene,[38] graphene/phosphorene,[43,44] and 2D-silicon/germanium[38] show higher energy storage capability compared to the individual building units that have been ascribed to the improvement of several physical properties such as the conductivity, surface area, increment of the layer to layer spacing, accommodation of a higher number of ions into the interlayers, or the appearance of favorable surface charge for ion intercalation. For example, MoS_2/graphene heterostructure shows a high capability of storing Na ions due to the enhanced conductivity of MoS_2 and high electron transfer efficiency from Na to MoS_2.[41] Rafieerad et al. fabricated germanane/MXene superlattice heterostructure “GerMXene” that showed excellent dispersibility and stability in aqueous media, high surface area, and negative surface charge.[45] Based on these studies, we anticipate that the heterostructure of GeH and MXene can be used as an electrode material having enhanced intercalation characteristics and higher energy storage capability in aqueous supercapacitors and batteries.

Herein, we report on 2D layered heterostructure of GeMXenes, assembling the delaminated GeH and $Ti_3C_2T_x$ 2D layers. The GeMXene heterostructure shows pseudocapacitive property through intercalation of cations that is confirmed by the density functional theory (DFT) calculation and EQCM[46–48] technique. The conductive MXene sheets mitigate the lower electrochemical performance of GeH, and the GeMXene heterostructure exhibits higher capacitive performance. A schematic presentation of GeMXene heterostructure preparation and the relative efficiency of ion intercalation is shown in **Scheme 1**. The stability and ion intercalation were examined in neutral salts, acidic, and alkaline mediums to comprehend the influence of cationic sizes and pH on the electrochemical performance. The study will unfold future directions of using GeMXene heterostructures as a potential negative electrode material for supercapacitors and batteries, taping synergistic effect of the individual components.

2. Results and Discussion

2.1. Physical Characterization

The GeMXenes heterostructures consist of delaminated 2D GeH and $Ti_3C_2T_x$ (hereafter referred as MXene) in the mass ratio of 1:1, 2:1, and 5:1, denoted as GeMXene-1, GeMXene-2, GeMXene-5. The successful preparation of the GeMXene heterostructure is verified from the structural analysis. The full X-ray diffraction (XRD) patterns of the delaminated GeH, MXene, and GeMXenes are shown in Figure S1 (Supporting Information). The diffraction peaks of GeMXenes inherit the peaks from both individual materials. The more interesting 2θ region of 5°–10° is depicted in **Figure 1**A. MXene shows its typical characteristic broad peak at 6.9° corresponding to the crystal plane (002) with a *d*-spacing of 12.64 Å. However, this peak is more refined and shifted to lower 2θ for GeMXenes. A larger peak shifting is observed with the increasing amount of GeH from GeMXene-1 to GeMXene-5. For GeMXene-2, a peak shifting of 1° to 2θ of 5.9° is noticed with an increase of *d*-spacing of 0.25 Å, where $d = 12.89$ Å. The expansion of *d*-spacing strongly indicates the interaction between 2D GeH and MXene heterolayers,[49] that is supported by DFT calculations as discussed in a later section.

Figure 1B depicts the Raman spectra of the delaminated GeH, MXene, GeMXene-1. GeMXene-2 and GeMXene-5 in the spectral region of 50–2400 cm^{-1}. The main characteristic peak of GeH at 293 cm^{-1} corresponds to the E_{2g} in-plane vibration of Ge—H bond.[12,50] Additionally, the other major peaks at 442 and 523 cm^{-1} are attributed to the symmetric stretching of Ge—O—Ge and Ge—Ge bond, respectively.[51–53] Besides, the small peaks at 95, 121, and 165 cm^{-1} correspond to the complex translation and rotation of the GeO_4 tetrahedra.[52] MXene shows peaks at 156, 400, and 625 cm^{-1} due to the presence of TiO_2 phase that is formed by partial oxidation of MXene surface during delamination in the aqueous phase.[54,55] Besides, the peaks of MXene at 1360 and 1556 cm^{-1} are attributed to the typical graphitic D-band and G-band structures,[55,56] with the intensity ratio of D-band to G-band

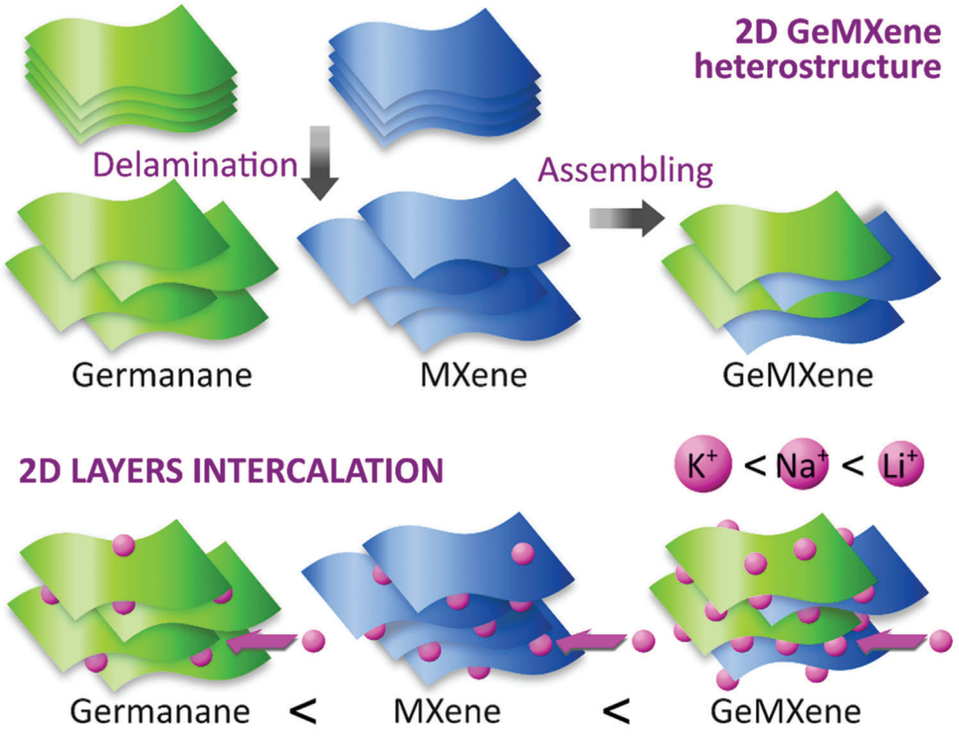

Scheme 1. Schematic presentation of the delamination of 2D germanane (GeH) and MXene ($Ti_3C_2T_x$) layers and assembling of GeMXene heterostructure. Investigation of ion intercalations in Germanane, MXene, and GeMXene layers.

(I_D/I_G) of 0.95. The GeMXenes inherit the characteristic peaks from GeH and MXene, however, the I_D/I_G ratios deviate from the MXene. The I_D/I_G ratio of GeMXene-2 is found to be 0.90. The increase in I_G can be attributed to the interaction between GeH and MXene heterolayers.[49]

A comparison of X-ray photoelectron spectroscopy (XPS) survey spectra for delaminated GeH, MXene, and GeMXene-2 is depicted in **Figure 2**A. GeH shows its characteristic peaks for Ge $2p_{3/2}/2p_{1/2}$ and Ge 3d at 1218/1251 and 33 eV, respectively. Besides, the C 1s and O 1s peaks are found at 285 and 530 eV, respectively. The MXene shows the peaks at 685, 530, 455, and 282 eV corresponding to the F 1s, O 1s, Ti 2p, and C 1s, respectively. The GeMXene-2 inherits the peaks from GeH and MXene. To investigate the bonding states of the elements in the heterostructure of GeMXene-2, the deconvoluted spectra (Ge 2p and Ti 2p) of the heterostructure are compared with GeH and MXene as depicted in Figure 2B,C, respectively. The deconvolution of Ge 2p reveals the peaks for Ge $2p_{3/2}$ of GeH at 1217.5, 1219.6, and 1220.6 eV, and the Ge $2p_{3/2}$ of GeMXene shows the peaks at 1217.5, 1218.6, and 1220.9 eV corresponding to GeH and GeO and GeO_2,

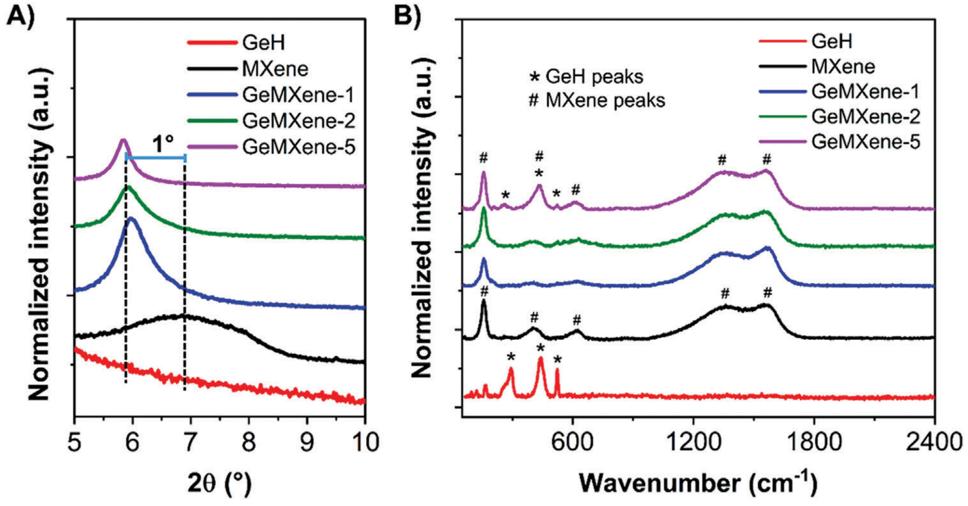

Figure 1. A) XRD patterns in 2θ in the 5°–10° region, and B) Raman spectra for delaminated GeH, MXene, GeMXene-1, GeMXene-2, and GeMXene-5.

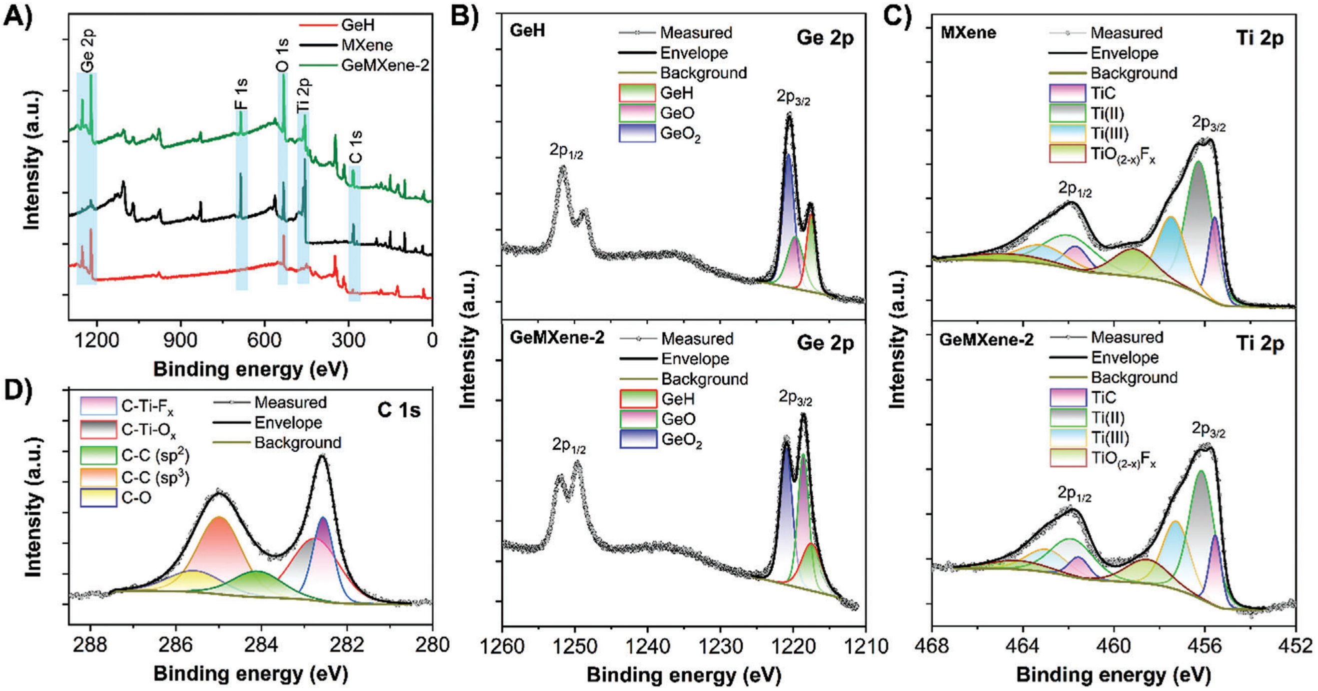

Figure 2. XPS analyses. A) Survey spectra of GeH, MXene ($Ti_3C_2T_x$), and GeMXene-2; high-resolution core-level spectra of B) Ge 2p of GeH and GeMXene-2, C) Ti 2p of MXene and GeMXene-2, and D) C 1s of GeMXene-2.

respectively. The intensity of the GeH peak is reduced, and the intensity of GeO and GeO_2 peaks increased in GeMXene-2. This implies the partial oxidation of GeH during the solution phase delamination, and the subsequent mixing step with MXene. The deconvolution of Ti 2p in GeMXene-2 shows the peaks at 455.5/461.5, 456.1/461.8, 457.2/562.9, and 458.5/464.2 eV corresponding to the Ti $2p_{3/2}/2p_{1/2}$ for Ti—C, Ti (II) and Ti (III) oxides, and $TiO_{2\text{-}x}F_x$ bonds, respectively, that originate from the $Ti_3C_2T_x$ MXene. The C 1s of GeMXene-2 in Figure 2D shows the peaks at 282.5, 282.7, 284.1, 284.9, 285.5 eV corresponding to the C—Ti—F_x, C—Ti—O_x, C—C (sp^2), C—C (sp^3), and C—O bonds, respectively, as identified in MXene in Figure S2 (Supporting Information).[57] Thus, XPS study confirms that GeMXene-2 possesses all the characteristic peaks from pristine GeH and MXene with a diminutive change of peak positions that can be attributed to the interlayer interactions between GeH and MXene. The interaction between GeH and MXene is analyzed in detail in Section 2.4 on Density functional theory (DFT) calculations.

Figure 3A,B presents the scanning electron microscopy (SEM) images of the as-received GeH and as-synthesized MXene. Both 2D materials exhibit the layered morphology, with GeH layers looking rigid and those of MXene appearing crumpled, in line with previous reports.[13,57,58] Figure 3C,D shows the SEM image of GeMXene-2. The contrast in Figure 3D taken by the circular backscatter (CBS) detector clearly indicates two different materials. The thin character of GeMXene-2 heterostructure is evidenced by the scanning transmission electron microscopy (STEM) images collected by bright field (BF) and high-angle annular dark-field (HAADF) detectors in Figure 3E,F, respectively. The X-ray energy dispersive spectroscopy (XEDS) elemental mapping in Figure 3G–J, in particular the overlay map shows that the overlapping Ge and Ti, evidencing the formation of the heterostructure.

The nitrogen adsorption/desorption isotherms GeH, MXene, and GeMXenes are displayed in Figure S3A (Supporting Information). The Brunauer–Emmett–Teller (BET) surface area of GeH, MXene, GeMXene-1, GeMXene-2, and GeMXene-5 is calculated to be 4.89, 11.67, 9.18, 6.70, and 5.64 $m^2\ g^{-1}$, respectively, and the Barrett–Joyner–Halenda (BJH) adsorption/desorption cumulative surface areas are determined to be 11.75/11.79, 27.19/26.93, 22.1/20.13, 17.1/17.36, and 15.85/15.57 $m^2\ g^{-1}$, respectively. From the BJH adsorption measurement, the pore size distribution as a function of the pore diameter is shown in Figure S3B (Supporting Information). The BJH adsorption cumulative pore volume of GeH, MXene, GeMXene-1, GeMXene-2, and GeMXene-5 are measured to be 0.024, 0.058, 0.044, 0.033, and 0.027 $cm^3\ g^{-1}$ and average adsorption pore diameter is 5.9, 11.76, 10.34, 8.23, and 7.46 nm, respectively. From the BET and BJH surface area and pore size distribution, it is found that MXene has the highest, while GeH has the lowest surface area. The surface areas of the GeMXenes stand in between the high and low values comprising the ratio of pristine materials. With increasing the ratio of GeH in the GeMXenes, the surface area and cumulative pore volume gradually decrease. This is attributed to the stacked 2D GeH layers (Figure 3A) with lower surface area and pore volume.

The electrical properties were determined by the van der Pauw 4-point resistivity method by applying 1 mA current. The surface resistivity of GeH, MXene, GeMXene-1, GeMXene-2, and GeMXene-5 are found to be 15.4×10^3, 45.4, 94.2, 96.8, and $3.9 \times 10^3\ \Omega\ cm^{-2}$. Clearly, MXene possesses the lowest resistivity and GeH the highest, and the GeMXenes are in between.

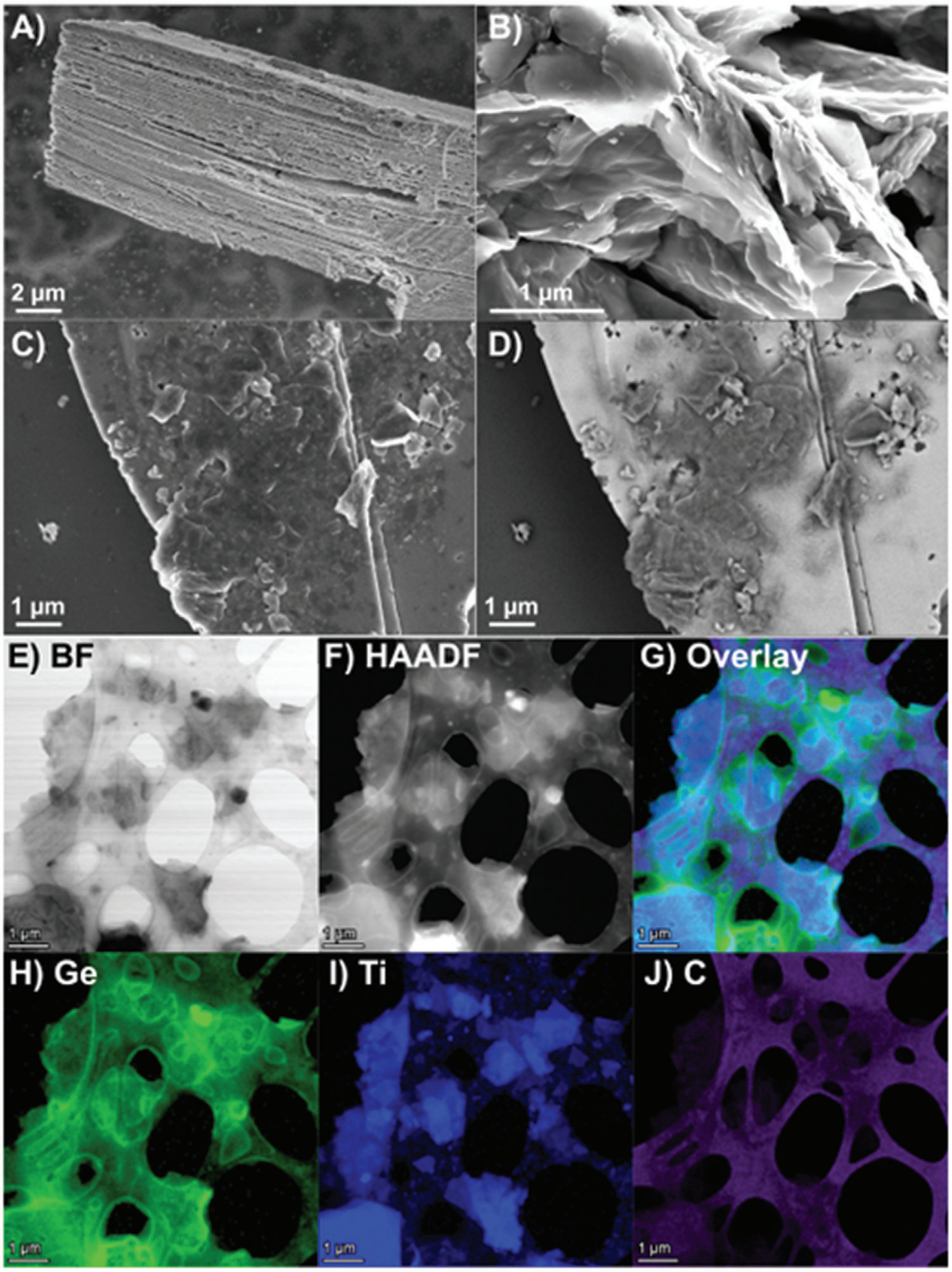

Figure 3. SEM images of A) GeH, B) MXene, C,D) GeMXene-2 by through-the-lens detector (TLD) and CBS detector, STEM images of GeMXene-2 (E,F) collected by BF, and HAADF detector, and STEM-XEDS maps of G) overlay of Ge, Ti and C, H–J) Ge, Ti, and C, respectively.

2.2. Electrochemical Study I — Comparison of Electrochemical Performances Among GeMXenes

Electrochemical studies were performed to investigate the interaction of different cations, namely Li^+, Na^+, and K^+, with the GeH, MXene, and GeMXenes samples. We started first with the LiCl electrolyte. The cyclic voltammetry (CV) studies of GeH, MXene, and GeMXene-2 at the scan rates from 10 to 100 mV s^{-1} are depicted in **Figure** 4A–C, GeMXene-1 and GeMXene-5 are shown in Figure S4A,B (Supporting Information). GeH shows a small potential window from −0.4 to 0 V with a quasi-rectangular pattern. MXene exhibits much higher specific current with the rectangular pattern at the potential window from −0.8 to +0.2 V. This implies that MXene has typical capacitive behavior with reversible ion adsorption and desorption. All GeMXenes exhibit the rectangular pattern similar to MXene at the same potential window from −0.8 to +0.2 V. For all GeMXenes, the current response increases with increasing the scan rates yet retains the same rectangular pattern. It is noteworthy that our electrode contains neither binder nor additional carbon black, which is typically used

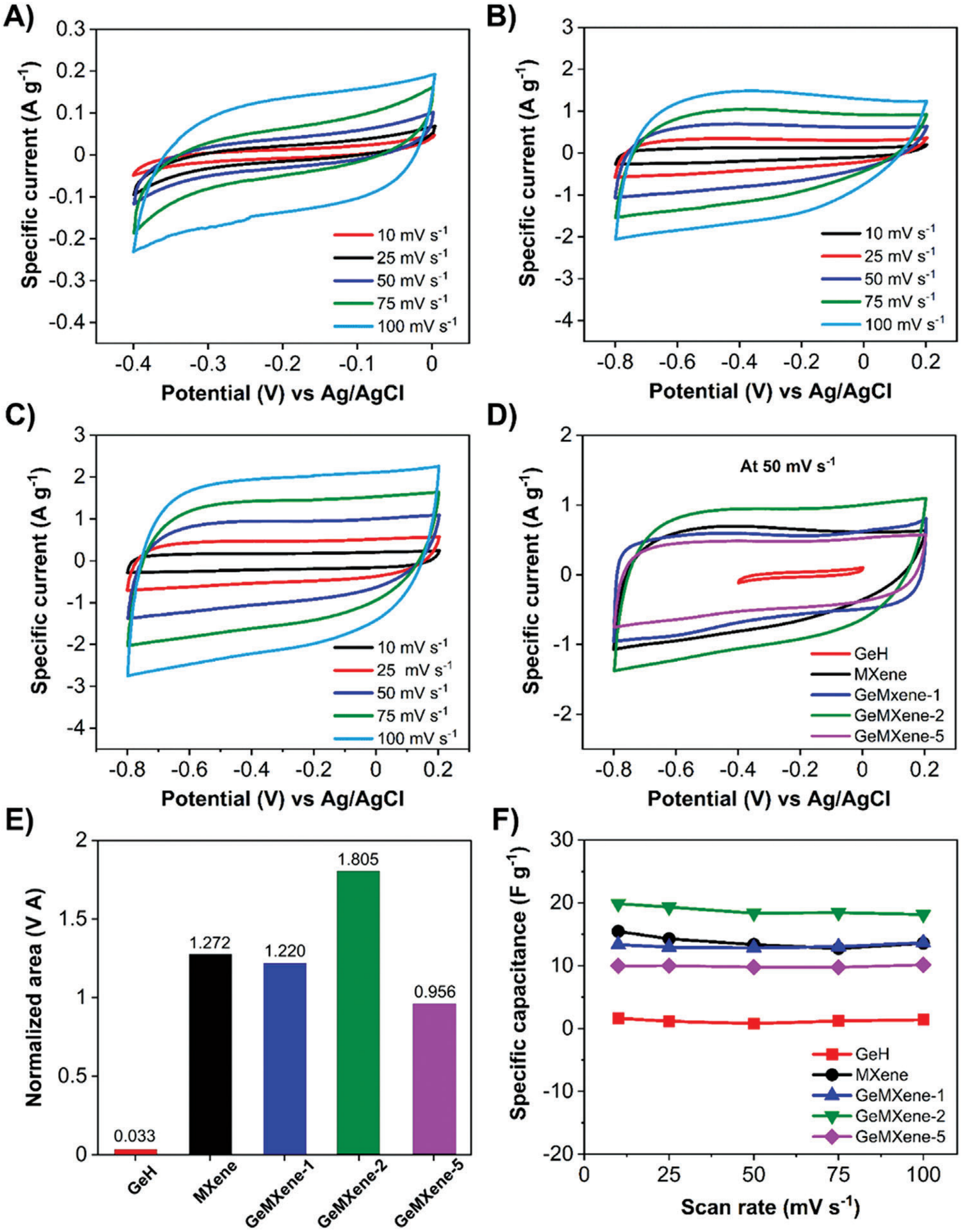

Figure 4. CV study in 1 M LiCl electrolyte at different scan rates of 10–100 mV s^{-1}. A) GeH, B) MXene, and C) GeMXene-2. D) Comparison of CV plots of GeH, MXene, and GeMXenes at 50 mV s^{-1}, E) comparison of the enclosed *I*–*V* area from CV plots at 50 mV s^{-1}, and F) comparison of specific capacitance of GeH, MXene, and GeMXenes at the scan rates of 10– 100 mV s^{-1}.

in battery and supercapacitor electrodes. Thus, the observed performances are fully attributable to the material(s) and are not influenced by any additives.

The electrochemical performances of the GeH, MXene, and GeMXenes are compared at the scan rate of 50 mV s^{-1} in Figure 4D to evaluate the best GeH:MXene ratio. The enclosed *I*–*V* areas normalized by the mass of the active materials are depicted in Figure 4E. Among all GeMXenes, GeMXene-2 shows the highest current responses and enclosed *I*–*V* area, hence the highest electrochemical performance. Separately, the specific capacitances for the scan rates of 10–100 mV s^{-1} were calculated by integrating the discharge area of the CV plots as shown in Figure 4F. It is seen that the GeMXene-2 shows 1.2 times higher capacitance than that of pristine MXene, and ≈12 times higher than that of GeH at the low scan rate of 10 mV s^{-1}. With the increase of the scan rate from 10 to 100 mV s^{-1}, the capacitance of GeMXene-2 becomes 1.4 times higher than that of pristine MXene and ≈13 times higher than that of GeH. This is attributed to the variation of capacitance with increasing the scan rate due to faster ion transport kinetics. The low specific capacitance of GeH is due to its low electrical conductivity. The higher capacitance of GeMXene-2 over MXene can be attributed to the heterolayer interaction between GeH and MXene that provides a favorable site for additional Li^{+} intercalation. This hypothesis is investigated by

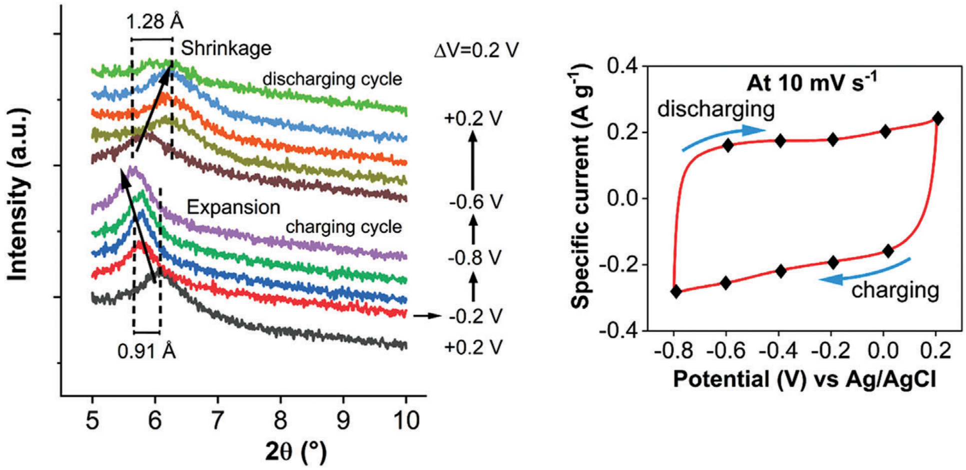

Figure 5. Ex situ XRD study of GeMXene-2 during CV charging and discharging processes. XRD pattern is taken at the 0.2 V interval starting from cathodic to anodic sweeping at the potential window from −0.8 to +0.2 V at the scan rate of 10 mV s^{-1}.

the DFT calculation in the later section. The GeMXene-5 exhibits lower performance than GeMXene-2 because of a higher mass ratio of GeH.

2.3. Electrochemical Study II — Cations Intercalation

Previous studies state that MXene exhibits intercalation of cations,[5] hence it is expected that GeMXenes will also show the reversible intercalation-deintercalation of ions in addition to the surface adsorption and desorption of ions. We perform the subsequent ions intercalation studies with GeMXene-2 in view of its highest electrochemical performance. To study the ion intercalation during CV study, we performed *ex situ* XRD analysis at several values of the potential during CV cycle (the spots marked in the CV plot in the inset of **Figure 5**), at the potential window from −0.8 to +0.2 V, starting at +0.2 V with cathodic sweep at the scan rate of 10 mV s^{-1}. The corresponding XRD patterns are shown in Figure 5. It is observed that the diffraction peak at 2θ of 5.9° (corresponding to the d-spacing of 14.89 Å) of the GeMXene-2 is gradually shifted toward lower 2θ during charging and toward the higher 2θ during discharging. This peak shifting from 5.9° to 5.6° clearly suggests that the d-spacing is increased during intercalation (charging) and decreased during de-intercalation (discharging) processes. Thus, it confirms that GeMXene-2 exhibits not only the electrochemical double-layer capacitance but also intercalation capacitance. This is in line with the previous study of cation intercalation of MXene.[5,33] Further analysis is elaborated in Section 2.4 on Density functional theory (DFT) calculations.

2.4. Density Functional Theory (DFT) Calculations

The materials analyses from XRD, Raman, XPS, and XEDS measurements presented in the previous section corroborate the formation of GeMXene heterostructure. In order to get atomic-scale details of the interface between GeH and MXene and model the effect of ion intercalation, we employ DFT calculations. The DFT calculations provide information on bonding characteristics on the heterostructure, interlayer distance, and scenarios for cation intercalation. The periodic supercell is used to model the GeMXene heterostructure. We find that the 3 × 3 supercell of the single layer GeH on top of the 4 × 4 $Ti_3C_2T_x$ provides a good match of the lattice parameters and hence minimizes an elastic strain within the heterostructure. We used O- and F-terminations of the surface of MXene as depicted in **Figure 6**A,B, respectively because our XPS survey identified peaks of both O 1s and F 1s in MXene. All atoms are allowed to fully relax.

Without the intercalated Li^+, GeH binds to MXene through weak van der Waals (vdWs) interaction only. To quantify the interaction, we calculated the surface energy of the interface, i.e., the energy needed to separate GeH from MXene. The resulting surface energies are 144 and 258 mJ m^{-2} for the F-terminated and O-terminated MXene, respectively. Such energies are typical for vdWs bonded systems such as graphite, graphite fluoride, TMDs etc.[59–61] Higher surface energy for the O-terminated surface stems for stronger electrostatic interaction at the interface. The interface is polarized; negative charge accumulates at H atoms of GeH while positive charge is induced on the O atoms at the MXene surface (Figure 6A). Moreover, charge accumulation appears in the interlayer region between the GeH layer and O-terminated MXene, indicating that the bonding is not purely of vdWs character. Stronger interlayer interaction of O-terminated MXene manifests itself by smaller interlayer distance in the heterostructure in comparison to that of F-terminated MXene. The density of states (DOS) around the Fermi level is dominated by d-orbitals of Ti hybridized with O and C p-orbitals, alongside the p-orbitals of Ge (Figure 6C). Compared to that, the change of charge density at the GeH interface with F-terminated MXene is weak (Figure 6B), which explains the lower surface energy of the GeMXene heterostructure.

When Li^+ cations intercalate into the structure, they provide better electronic coupling of heterostructure. Li^+ cation binds primarily at the MXene surface, sitting at the hollow site between O/F atoms terminating MXene layer (Figure 6D,E). The Li—F bond length is 2.00 Å. For GeH, Li^+ accommodates preferentially the hollow sites farther from H atoms. Strong charge accumulation appears in the interfacial region in the vicinity of the

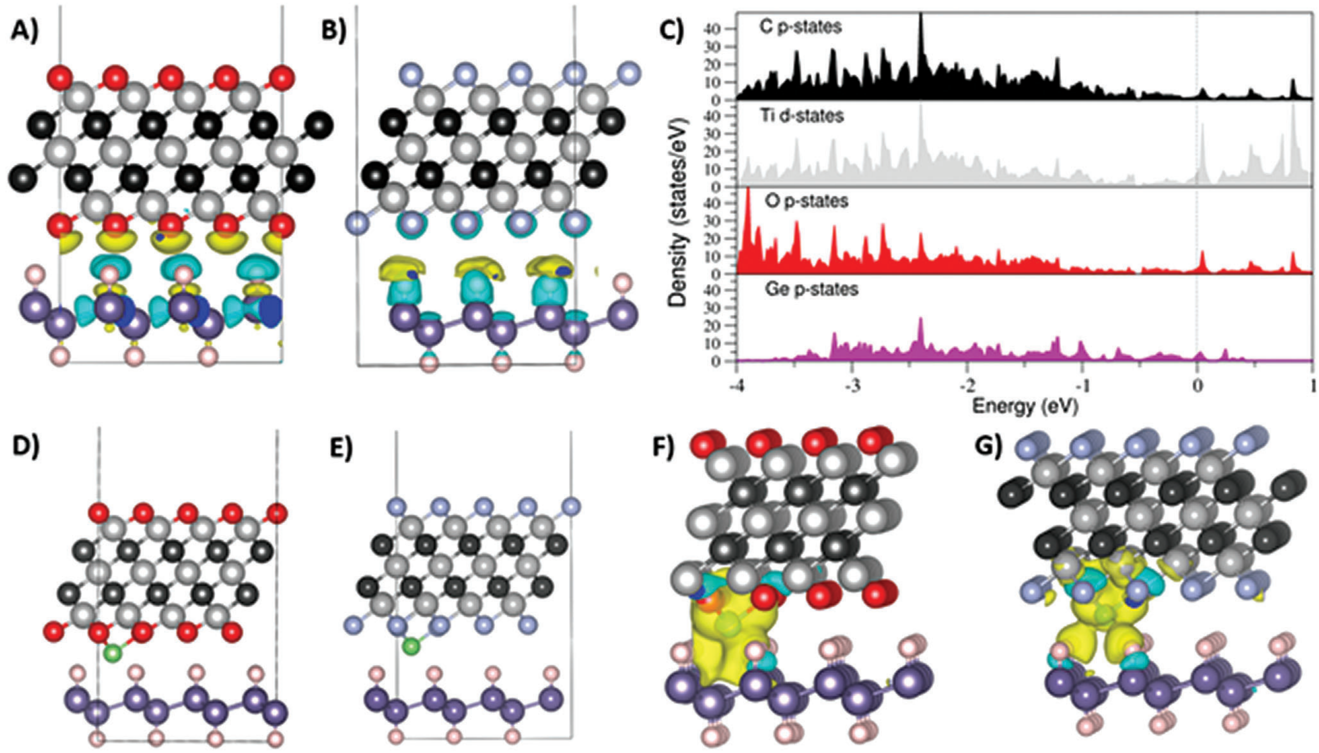

Figure 6. Theoretical calculations of GeMXene. The supercell models of GeMXene and the charge density induced at the interface for A) O-terminated MXene, B) F-terminated MXene; C) projected density of states of O-terminated GeMXene. The structure of the interface having intercalated Li^+ cation for D) the O-terminated MXene and E) F-terminated MXene; the charge density induced at the GeH-MXene interface by intercalation of Li^+ cation for F) the O-terminated MXene and G) F-terminated MXene. Colors: negative induced charge = cyan, positive induced charge = yellow. Atoms color for GeH: Ge = violet, H = light pink; and for $Ti_3C_2T_x$ MXene: Ti = grey, C = dark grey, O = red, F = light blue, and Li = green.

intercalated Li^+, in particular for O-terminated MXene (Figure 6F). The charge induced in the region between GeH and MXene indicates that the intercalated Li^+ can serve as a bridge between the GeH and MXene, boosting the charge transfer across the GeMXene heterostructure.

To quantify the likelihood of Li^+ intercalation, we calculated the formation energy of intercalated Li^+ cations (i.e., the intercalation energy). The DFT intercalation energy, E_{int} was calculated according to Equation (1).

$$E_{\mathrm{int}} = \frac{E_{\mathrm{GeMXene}/n\mathrm{Li}} - \left(E_{\mathrm{GeMXene}} + n_{\mathrm{Li}}\mu_{\mathrm{Li}}\right)}{n_{\mathrm{Li}}} \tag{1}$$

where, $E_{\mathrm{GeMXene}/n\mathrm{Li}}$ is the total energy of the GeMXene heterostructure with n intercalated Li^+ cations (n_{Li}), E_{GeMXene} is the energy of Li^+ ion-free heterostructure and μ_{Li} is the chemical potential of Li^+. To mimic the experimental conditions, we select the total energy of isolated Li^+ cations plus the solvation energy of Li^+ in water as the reference energy for μ_{Li}. **Table 1** lists the calculated E_{int} for the intercalation of Li^+ (in different fractions of mass) into GeMXene, with O-terminated and F-terminated MXenes.

The intercalation is feasible at the O-terminated GeMXene. At low number of Li^+ cations, the intercalation energy is negative, i.e., intercalation is exothermic and should proceed spontaneously. As the number of Li^+ increases, the intercalation energy increases due to the electrostatic repulsion between Li^+ cations. The fully intercalated heterostructure, defined by 1:1 ratio between Li^+ and surface O atoms, has positive intercalation energy of 0.5 eV. We note that the intercalation energy is directly related to the intercalation potential, V_{int} given by Equation (2).[62,63]

$$V_{\mathrm{int}} = \frac{-E_{\mathrm{int}}}{n_{\mathrm{Li}}\ F} \tag{2}$$

where V_{int} is related to the Li^+ (de)intercalation at different (de)intercalation potentials in charge–discharge cycle (CV in Figure 5). Based on the calculated values of E_{int}, even without applying potential, the concentration of Li^+ in the

Table 1. The formation energy of Li^+ intercalation into GeMXene heterostructures with O-terminated and F-terminated MXene. The number n of the intercalated Li^+ cations is given as a fraction of O/F atoms terminating MXene. See text for details of the calculation.

n_{Li}	E_{int} [eV]
O-terminated	
1/16	−0.42
1/8	−0.33
1	0.50
F-terminated	
1/16	1.02

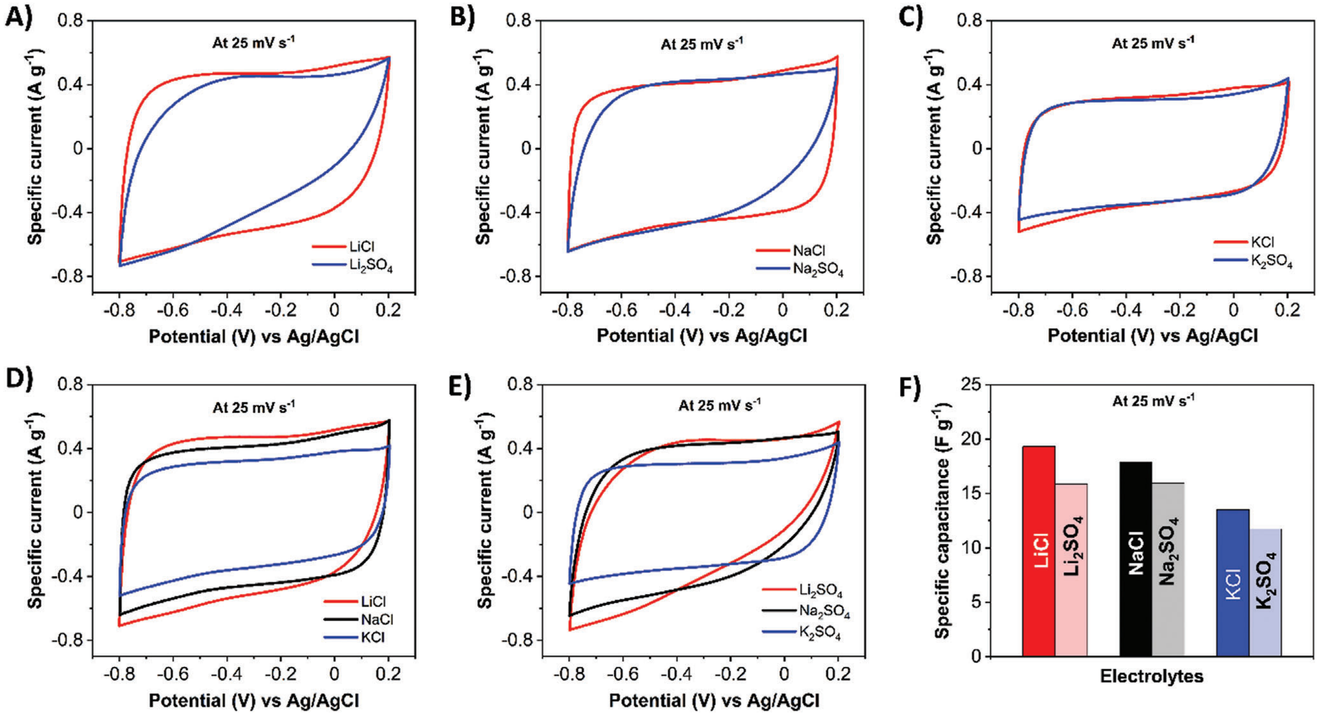

Figure 7. CV study of GeMXene-2 at the scan rate of 25 mV s^{-1}. A–C) Comparison of the effect of anions in Li, Na, and K salts. D,E) Comparison of cations size for Cl$^-$ and SO$_4$$^{2-}$ -based electrolyte. F) Comparison of the capacitance performance of GeMXene-2 in LiCl, NaCl, KCl, Li$_2$SO$_4$, Na$_2$SO$_4$, and K$_2$SO$_4$ at the scan rate of 25 mV s^{-1}.

GeMXene is in a certain equilibrium. This concentration is then increased during intercalation (charging) until a fully intercalated Li layer is formed (n Li$^+$ = 1), and decreased while deintercalation (discharging). The interlayer separation between GeH and MXene (measured as the distance between the H layer of GeH and the surface Ti layer of MXene) increases from 3.34 Å (Li$^+$-free heterostructure) to 3.68 Å (fully Li$^+$-intercalated). This value is lower than the increase observed experimentally (see previous Section 2.3, Electrochemical Study II – Cations Intercalation). We assume that during the experiment, the solvated Li$^+$ carries additional water molecules into the heterostructure and these molecules increase the interlayer separation. Further details are in Section 2.6 of Electrochemical Study IV.

2.5. Electrochemical Study III – Effect of Cationic and Anionic Size Toward Electrochemical Performance

To confirm the contribution of cationic (Li$^+$) intercalation toward the electrochemical performances of GeMXene-2, we studied the Li salts by varying the anions (Cl$^-$ and SO$_4$$^{2-}$). The CV plots in **Figure 7**A at the scan rate of 25 mV s^{-1} show only a minor deviation between LiCl and Li$_2$SO$_4$ electrolytes. We extended the evaluation for Na$^+$ in NaCl and Na$_2$SO$_4$, and K$^+$ in KCl and K$_2$SO$_4$. Similarly to Li$^+$, only a slight deviation in CV plots was observed for Na$^+$ and K$^+$, with different anionic counterparts as shown in Figure 7B,C. While we present only the CV plots of scan rate 25 mV s^{-1}, the CV plots at other scan rates in all the electrolytes are shown in Figures S5 and S6 (Supporting Information). This set of measurements also allows us to compare the effect of the size of cations (Li$^+$, Na$^+$, and K$^+$). Figure 7D,E shows a comparison of CV plots among Li$^+$, Na$^+$, and K$^+$ ions in Cl$^-$ and SO$_4$$^{2-}$ salts electrolytes, respectively, and Figure 7F compares the calculated specific capacitances for all the aqueous salt electrolytes at the scan rates of 25 mV s^{-1}. In Cl$^-$ salt electrolytes, the highest performance is recorded in Li$^+$ electrolytes, followed by Na$^+$ and K$^+$ electrolytes. In SO$_4$$^{2-}$ salt electrolytes, a similar performance is found in Li$_2$SO$_4$ and Na$_2$SO$_4$ electrolytes, followed by a lower performance in K$_2$SO$_4$ electrolytes. The specific capacitance of a 2D material in the aqueous electrolytes of alkali metal salts with a similar anionic counterpart depends on several factors, such as the radius of the bare cations, hydrated cationic radius, ionic mobility, molar conductivity, their effect on charge/ion diffusion, and interactions between the cations and the 2D material surface.[64–66] The ionic radii of Li$^+$ (0.94 Å) < Na$^+$ (1.17 Å) < K$^+$ (1.49 Å) whereas the hydrated ionic radii are Li$^+$ (3.83 Å) > Na$^+$ > (3.58 Å) > K$^+$ (3.31 Å) owing to their different charge densities.[67] Besides, the molar conductivity and ionic mobility of cations are in the order of Li$^+$ < Na$^+$ < K$^+$.[68] During the charge/discharge process, bare cations and H$_2$O molecules can also be inserted/deinserted along with the hydrated cations.[69] The smaller ionic radius eases more ion insertion within the GeMXene-2 layers facilitating higher charge transfer, while higher conductivity and mobility of ion aids faster transfer of ions. Moreover, the interactions of ions with the GeMXene-2 surface termination play a significant role in the ion intercalation process. The intercalated water mobility is also affected by its interaction with surface termination groups of

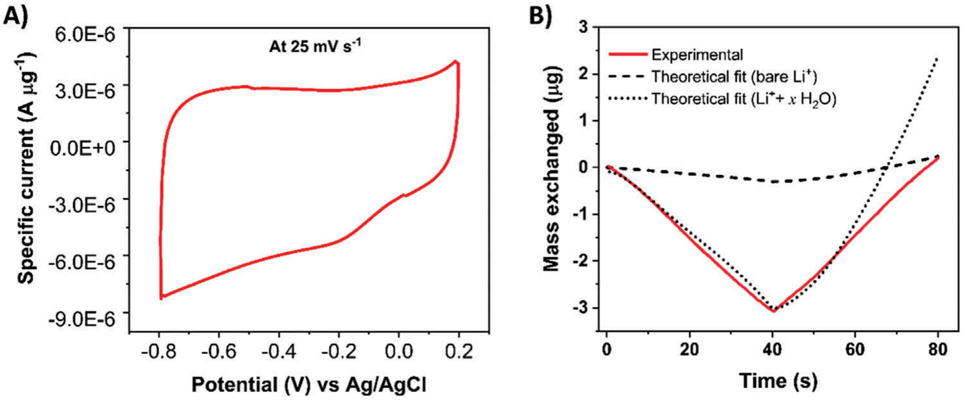

Figure 8. EQCM measurement of GeMXene-2 in 1 м LiCl electrolyte, A) CV plot, and B) mass exchanged profile.

GeMXene-2.[66] The specific capacitances in Cl^- salt electrolytes ($Li^+ > Na^+ >$ and K^+) and SO_4^{2-} salt electrolytes ($Li^+ \approx Na^+ > K^+$) suggest that effects from the inserted hydrated and bare cations, their ionic mobilities, and the cation-water-GeMXene and cation-GeMXene interactions combine and cause observed order of capacitances.[64,66,70] Comparing the similar cationic sizes, there is only a slight variation of capacitance between Cl^- and SO_4^{2-} salts. This is attributed to the size of anions and their ionic mobilities that play a diminutive effect on ion intercalation.[32]

2.6. Electrochemical Study IV — Electrochemical Quartz Crystal Microbalance (EQCM) Analysis

The real-time monitoring of the mass exchange in the GeMXene-2 heterostructure during CV study was measured by the EQCM. The exchange of ions and water molecules can be determined during the electrochemical process, employing the Sauerbrey equation (Equation (3)).[71–73]

$$\Delta m = -C_f \frac{\Delta f}{n} \tag{3}$$

where Δm = mass exchange, C_f = calibration constant (17.7 ng cm^{-2} Hz^{-1}), Δf = frequency change and n = number of harmonic (n = 1, 3, 5,..). For each CV cycle, the system records the corresponding response of Δf, and the Δm of the GeMXene-2 in a CV cycle can be calculated using Equation (3). **Figure 8**A,B depicts the CV plot and its corresponding mass exchange profile (for n = 1) of the GeMXene-2 in 1 м LiCl electrolyte solution, respectively. In Figure 8B, the experimental curve represents the exchange of specifically cationic species during the charge–discharge cycle. Further, a theoretical fitting is plotted considering the exchange of bare Li^+ cations (the molar mass of Li^+ = 7 g mol^{-1}) only. Interestingly, it is found that the experimental mass exchange is higher than the theoretical fit with bare Li^+ cations. Hence, the excess mass can be accounted for the water molecules in the electrolyte, which are exchanged either as hydrated Li^+ or in free form. Considering the sum of the molar mass of ions and water molecules exchanged, a new fitting line is added in Figure 8B, denoted as theoretical fit ($Li^+ + x\ H_2O$)). The amount of water molecules exchanged during the electrochemical process is calculated using Equation (4).

$$\text{Water exchanged } (x) = \frac{M_{\text{theoretical fit } (Li^+ + xH_2O)} - M_{\text{theoretical fit } (Li^+)}}{M_{H_2O}} \tag{4}$$

where, $M_{\text{theoretical fit } (Li^+ + xH_2O)}$ = sum of the molar mass of exchanged species (ions and water molecules), $M_{\text{theoretical fit } (Li^+)}$ = molar mass of respective cations in the systems (Li^+), M_{H_2O} corresponds to the molar mass of water (18 g mol^{-1}).

Employing Equation (4), the water molecules exchanged per Li^+ cation are found to be 3.5. In short, it is evident that ($Li^+ + x\ H_2O$) species are exchanged during the charge–discharge process in the GeMXene-2 electrode material, supporting the DFT calculation.

2.7. Electrochemical Study V — Effect of pH Toward Electrochemical Performance

We analyze the electrochemical performance of GeMXene-2 in alkaline and acid electrolytes to investigate the effect of pH. The CV plots of GeMXene-2 in 1 м NaOH and KOH electrolytes at the scan rates from 10 to 100 mV s^{-1} are shown in **Figure 9**A and Figure S7 (Supporting Information), respectively. The CV plots show a stable potential window from −1.0 to 0 V. The potential window differs from the neutral salt electrolytes (−0.8 to +0.2 V). Besides, the CV plots deviated from the rectangular shape. Clearly, the pH of the electrolyte affects the cathodic and anodic paths. Subsequently, the CV study was carried out in an acidic electrolyte of 1 м of H_2SO_4. The GeMXene-2 shows the capacitive potential range from −0.4 to +0.2 V with a smaller capacitive potential window of 0.6 V as depicted in Figure 9B, instead of 1.0 V for neutral salts and alkaline electrolytes. The CV plots show a typical quasi-rectangular shape. The electrode shows a specific capacitance of 31 F g^{-1} at the scan rate of 10 mV s^{-1}. We further compare the role of cationic size in the alkaline medium in Figure 9C. The same trend is observed as for neutral electrolytes, where smaller cationic sizes delivered higher electrochemical performance. A final comparison of the capacitive performance in neutral (LiCl), acidic (H_2SO_4), and alkaline (NaOH) electrolytes is shown in Figure 9D. GeMXene-2 provides

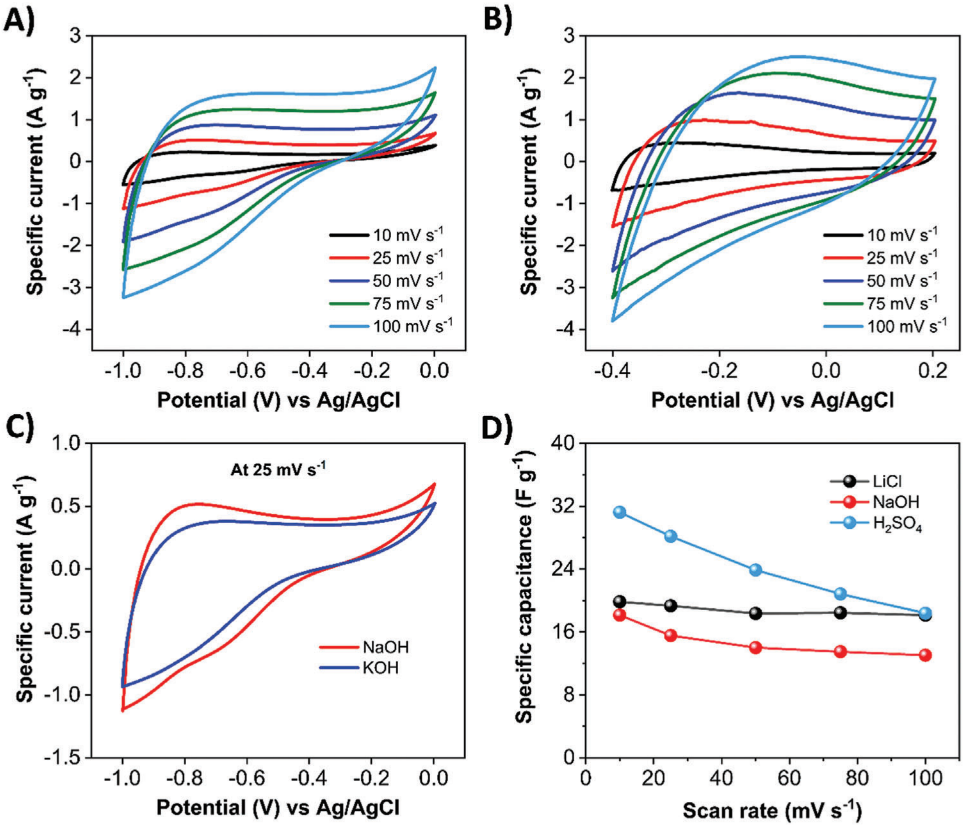

Figure 9. CV study in A) NaOH and B) H_2SO_4 electrolyte at the scan rate 10–100 mV s^{-1}, C) comparison of CV plots in NaOH and KOH electrolyte at 25 mV s^{-1}, D) comparison of capacitance in 1 M LiCl, NaOH, and H_2SO_4 electrolytes at different scan rates.

the highest capacitance in the H_2SO_4 electrolyte. The higher capacitance of GeMXene-2 in the acidic medium can be attributed to the higher intercalation of hydrated H^+ in the heterostructure layers.

2.8. Electrochemical Study VI – Cyclic Stability

Further, the cyclic performance of GeMXene-2 was evaluated in 1 M LiCl electrolyte by employing CV for 5000 cycles at the scan rate of 50 mV s^{-1}. The capacitance retention against cycle number is depicted in **Figure 10** and the CV plot of every 200 cycles is shown as an inset in Figure 10. The enclosed area is apparently decreased with increasing the cycles. However, it shows a reasonable ≈92% capacitance retention after 5000 cycles.

3. Conclusion

We fabricated the heterostructure of 2D GeH and MXene $Ti_3C_2T_x$ called "GeMXene" that shows superior capacitive performance surpassing that of both pristine materials at a defined mass ratio of individual components. We carried out a complete materials analysis of the GeMXenes relative to parent materials. GeMXene with the mass ratio of GeH to MXene 2:1 promotes the intercalation of cations between the heterolayers and exhibits the highest capacitive performance. We performed a systematic electrochemical investigation in different electrolyte systems to study the influence of the size of cations (Li^+, Na^+, and K^+) and anions (Cl^-, OH^-, and SO_4^{2-}), and pH of the electrolyte

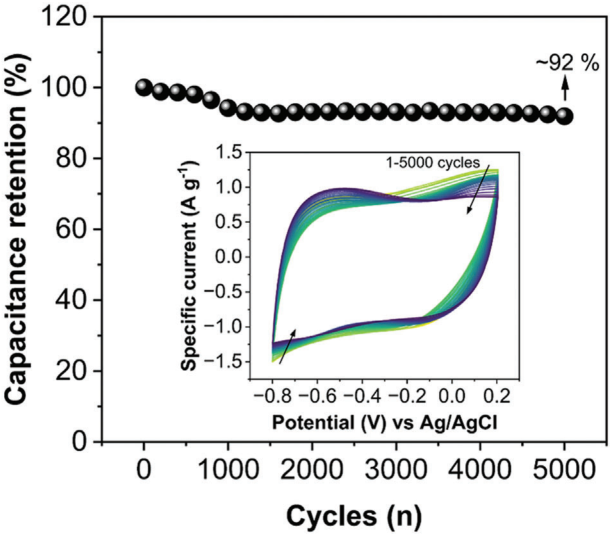

Figure 10. Cyclic stability test. Capacitance retention for 5000 cycles of CV scans in 1 M LiCl electrolytes. Inset: CV for 5000 scans at 50 mV s^{-1}, plots displaying at 200 cycles intervals from 1 to 5000 cycles.

(neutral, acidic, and alkaline). Among all the tested electrolytes, GeMXene presents the highest capacitive performance for cations of smaller atomic size and in acidic electrolytes. The intercalation of Li^+ ions between the heterolayers of GeMXene is evidenced by experimental and theoretical studies. *Ex situ* XRD study during the charge–discharge cycle shows that increment of *d*-spacing during intercalation and decrement during deintercalation. The electrochemical quartz crystal microbalance (EQCM) study confirms the exchange of Li^+ along with water molecules into the GeMXene during the charge–discharge process. Density Functional Theory (DFT) calculations show the favorable thermodynamic states of Li^+ ion intercalation in GeMXene layers, especially for O-terminated MXene layers. The work presents an improved capacitive performance by a heterostructure constructed from the 2D Germanane and MXene ($Ti_3C_2T_x$ with O/F-termination). Beyond GeMXene, the synergism of the 2D van der Waals (vdW) heterostructures based on other materials such as functionalized Xanes and other MXenes can be explored as potential electrodes for electrochemical energy storage systems, such as supercapacitors, batteries, and hybrid batteries.

4. Experimental Section

Materials: Lithium chloride (LiCl), sodium chloride (NaCl), potassium chloride (KCl), lithium sulfate (Li_2SO_4), sodium sulfate (Na_2SO_4), potassium sulfate (K_2SO_4), sulfuric acid (H_2SO_4), sodium hydroxide (NaOH), and potassium hydroxide (KOH) were purchased from Merck, Germany. All materials were purchased as an analytical grade. Besides, Germanane (GeH) was also procured by Merck, Germany.

Preparation of 2D GeH/$Ti_3C_2T_x$ (GeMXene) Heterostructure: $Ti_3C_2T_x$ MXene was synthesized according to the previous work.[57,58] For the delamination process, $Ti_3C_2T_x$ and GeH were separately dispersed in a mixture of water and ethanol (ratio 1:1) and ultrasonicated in a water bath for 15 and 5 min, respectively. Three different concentrations of GeMXenes were prepared by mixing the delaminated GeH and $Ti_3C_2T_x$ in the ratio of 1:1, 2:1, and 5:1. The concentration of the resulting suspension was 1, 1.5 and 3 mg mL^{-1}, respectively. The dispersions were bath sonicated for 1 min and placed in a vortex shaker for 24 h to allow the interaction of both materials. The resulting mixtures were denoted according to the concentration of GeH, i.e., GeMXene-*n* where $n = 1$, 2, and 5.

Materials Characterizations: GeMXene was imaged by SEM Verios 460L, (Thermo Fisher Scientific) equipped with a TLD, CBS, and STEM detector in bright-field mode. The STEM-BF and -HAADF imaging and STEM-XEDX elemental mapping were performed with a TITAN Themis 60–300 microscope (Thermo Fischer Scientific) operated at 300 keV and equipped with Super-X XEDS spectrometer. The presented elemental maps were taken from C-K, Ti-K, and Ge-K lines and performed in the form of their net intensities. All TEM data acquisition and processing was done with the software Velox. Structural analyses were performed by XRD using a diffractometer (SmartLab 3 kW, Rigaku) with Bragg–Brentano geometry. A Cu lamp was operated at a current of 30 mA and a voltage of 40 kV with Cu Kα radiation ($\lambda = 1.54$ Å) equipped by 1D-detector Dtex-Ultra. Chemical compositional analyses with XPS were carried out by AXIS Supra spectrometer (Kratos Analytical) using a monochromatic Al Kα (1486.7 eV) X-ray excitation source with power of 225 W. The Raman spectra acquisition was conducted with an Alpha 300R Raman microscope (WITec) using a laser excitation source ($\lambda = 532$ nm) with a power of 25 mW. Electrical resistivity was measured by a four-probe electrical workstation (Cascade Microtech MPS 150) with a source measuring unit (SMU, Keithley 4200-SCS Parameter Analyzer). The BET surface area measurement was carried out by measuring adsorption/desorption isotherm using the Micro 300 C1 (3P Instrument, BET-ANAMET) surface area analyzer. All the samples were degassed at 50 °C for 20 h prior to the surface area measurement. Nitrogen was used as adsorbate and the bath temperature was kept ≈77 K. The BET surface area was calculated employing BET equation for relative pressure (p/p_0) range of 0.1–0.3, and the BJH pore size distribution was determined from the adsorption/desorption isotherm p/p_0 of 0.35–1.0 range.

Density Functional Theory (DFT) Calculations: DFT calculations were performed using the projector-augmented wave method in the Vienna Ab initio Simulation Package (VASP) suite.[74,75] The energy cutoff for the plane-wave expansion was set to 400 eV. The interaction energy and forces were calculated using optimized van der Waals functional optB86b-vdW.[76] This function provided excellent results in previous studies of materials combining covalent, ionic, and vdWs bonding.[77]

Electrochemical Measurements: The as-prepared GeH, MXene, and GeMXene-*n* dispersions were centrifuged to collect a concentrated solution of 25 mg mL^{-1} and then drop-casted on stainless steel foil of 0.5 × 1 cm^2 area. Note that no binder and conductive carbon black were used to prepare the electrodes. The mass of the deposited sample was calculated by the gravimetric method. For the electrochemical study, CV study was carried out employing a potentiostat (Metrohm Autolab, PGSTAT 204, Netherlands) with Nova 2.1 software using Ag/AgCl (1 M KCl) as a reference electrode and Pt wire as a counter electrode. The CV study was carried out in neutral, acidic, and alkaline electrolytes starting at open-circuit potential (OCP) followed by a cathodic sweep. Prior to the cyclic stability test, the GeMXene was run for 50 cycles. The specific capacitance was calculated using Equation S1 (Supporting Information).

For the EQCM measurements, a 5 MHz Au-coated QCM sensor was employed. GeMXene-2 (1.5 mg mL^{-1}) was spray coated on the Au-QCM, dried completely in an electric oven at 50 °C, and used as the working electrode. Here, the mass loading per geometric surface area is much lower than the normal CV measurement. The frequency of quartz before and after loading was recorded. The EQCM measurements followed the three-electrode configuration and electrochemical conditions mentioned above. The CV measurement was cycled multiple times to improve the wettability and electrochemical stability of the system.

Supporting Information

Supporting Information is available from the Wiley Online Library or from the author.

Acknowledgements

K.G. acknowledges the funding from the European Union's Horizon 2020 research and innovation programme under the Marie Skłodowska-Curie grant agreement No (894457-MotionESt). M.P. and P.L. acknowledge the support from ERDF/ESF project TECHSCALE (No. CZ.02.01.01/00/22_008/0004587). Authors thank CzechNanoLab Research Infrastructure LM2023051, funded by MEYS CR for materials characterizations. This research was co-funded by the European Union under the REFRESH-Research Excellence For REgion Sustainability and High-tech Industries project number CZ.10.03.01/00/22_003/0000048 via the Operational Programme Just Transition. Typographical errors in the text and Figures 9 and 10 were corrected after initial online publication.

Conflict of Interest

The authors declare no conflict of interest.

Author Contributions

K.G. and S.N. contributed equally to this work. K.G. conceptualized the work. K.G. and S.N. synthesized the GeMXene. S.N. carried out materials characterization and analysis. K.G. conducted electrochemical performance and analysis. P.L. conducted theoretical calculation and analysis. A.K.K.P. carried out the EQCM study and analysis. J.M. performed STEM imaging and STEM-XEDS chemical composition measurement and analysis. M.P. supervised the research. All authors contributed to the writing.

Data Availability Statement

The data that support the findings of this study are available from the corresponding author upon reasonable request.

Keywords

energy storage, GeH, heterostructures, supercapacitor, $Ti_3C_2T_x$, Xenes

Received: July 27, 2023
Revised: October 11, 2023

[1] J. R. Miller, P. Simon, *Science* **2008**, *321*, 651.
[2] P. Simon, Y. Gogotsi, *Nat. Mater.* **2008**, *7*, 845.
[3] M. Xu, T. Liang, M. Shi, H. Chen, *Chem. Rev.* **2013**, *113*, 3766.
[4] K. S. Kumar, N. Choudhary, Y. Jung, J. Thomas, *ACS Energy Lett.* **2018**, *3*, 482.
[5] M. R. Lukatskaya, O. Mashtalir, C. E. Ren, Y. Dall'agnese, P. Rozier, P. L. Taberna, M. Naguib, P. Simon, M. W. Barsoum, Y. Gogotsi, *Science* **2013**, *341*, 1502.
[6] Q. Yun, L. Li, Z. Hu, Q. Lu, B. Chen, H. Zhang, *Adv. Mater.* **2020**, *32*, 1903826.
[7] L. Lin, W. Lei, S. Zhang, Y. Liu, G. G. Wallace, J. Chen, *Energy Storage Mater.* **2019**, *19*, 408.
[8] T. Giousis, G. Potsi, A. Kouloumpis, K. Spyrou, Y. Georgantas, N. Chalmpes, K. Dimos, M.-K. Antoniou, G. Papavassiliou, A. B. Bourlinos, H. J. Kim, V. K. S. Wadi, S. Alhassan, M. Ahmadi, B. J. Kooi, G. Blake, D. M. Balazs, M. A. Loi, D. Gournis, P. Rudolf, *Angew. Chem.* **2021**, *133*, 364.
[9] S. Ng, M. Pumera, *Adv. Mater.* **2022**, *35*, 2207196.
[10] L. C. Yang, Q. S. Gao, L. Li, Y. Tang, Y. P. Wu, *Electrochem. Commun.* **2010**, *12*, 418.
[11] X. Xiao, X. Li, S. Zheng, J. Shao, H. Xue, H. Pang, *Adv. Mater. Interfaces* **2017**, *4*, 1600798.
[12] A. C. Serino, J. S. Ko, M. T. Yeung, J. J. Schwartz, C. B. Kang, S. H. Tolbert, R. B. Kaner, B. S. Dunn, P. S. Weiss, *ACS Nano* **2017**, *11*, 7995.
[13] S. Ng, J. Sturala, J. Vyskocil, P. Lazar, J. Martincova, J. Plutnar, M. Pumera, *ACS Nano* **2021**, *15*, 11681.
[14] S. Jiang, S. Butler, E. Bianco, O. D. Restrepo, W. Windl, J. E. Goldberger, *Nat. Commun.* **2014**, *5*, 3389.
[15] J. Sturala, J. Luxa, S. Matejková, J. Plutnar, T. Hartman, M. Pumera, Z. Sofer, *Chem. Mater.* **2019**, *31*, 10126.
[16] C. Livache, B. J. Ryan, U. Ramesh, V. Steinmetz, C. Gréboval, A. Chu, T. Brule, S. Ithurria, G. Prévot, T. Barisien, A. Ouerghi, M. G. Panthani, E. Lhuillier, *Appl. Phys. Lett.* **2019**, *115*, 052106.
[17] Y. J. Cho, H. S. Im, H. S. Kim, Y. Myung, S. H. Back, Y. R. Lim, C. S. Jung, D. M. Jang, J. Park, E. H. Cha, W. I. Cho, F. Shojaei, H. S. Kang, *ACS Nano* **2013**, *7*, 9075.
[18] K. H. Seng, M.-H. Park, Z. P. Guo, H. K. Liu, J. Cho, *Angew. Chem.* **2012**, *124*, 5755.
[19] Y. Xiao, M. Cao, L. Ren, C. Hu, *Nanoscale* **2012**, *4*, 7469.
[20] B. Wu, J. Sturala, M. Veselý, T. Hartman, E. Kovalska, D. Bouša, J. Luxa, J. Azadmanjiri, Z. Sofer, *Nanoscale Adv.* **2021**, *3*, 4440.
[21] R. A. Dileo, M. J. Ganter, B. J. Landi, R. P. Raffaelle, *J. Mater. Res.* **2010**, *25*, 1441.
[22] D. Li, K. H. Seng, D. Shi, Z. Chen, H. K. Liu, Z. Guo, *J. Mater. Chem. A* **2013**, *1*, 14115.
[23] J.-G. Ren, Q.-H. Wu, H. Tang, G. Hong, W. Zhang, S.-T. Lee, *J. Mater. Chem. A* **2013**, *1*, 1821.
[24] X. Gao, W. Luo, C. Zhong, D. Wexler, S.-L. Chou, H.-K. Liu, Z. Shi, G. Chen, K. Ozawa, J.-Z. Wang, *Sci. Rep.* **2014**, *4*, 6095.
[25] M. Alhabeb, K. Maleski, B. Anasori, P. Lelyukh, L. Clark, S. Sin, Y. Gogotsi, *Chem. Mater.* **2017**, *29*, 7633.
[26] Z. Lin, H. Shao, K. Xu, P.-L. Taberna, P. Simon, *Trends Chem.* **2020**, *2*, 654.
[27] M. R. Lukatskaya, S. Kota, Z. Lin, M.-Q. Zhao, N. Shpigel, M. D. Levi, J. Halim, P.-L. Taberna, M. W. Barsoum, P. Simon, Y. Gogotsi, *Nat. Energy* **2017**, *2*, 17105.
[28] M.-Q. Zhao, X. Xie, C. E. Ren, T. Makaryan, B. Anasori, G. Wang, Y. Gogotsi, *Adv. Mater.* **2017**, *29*, 1702410.
[29] A. Byeon, M.-Q. Zhao, C. E. Ren, J. Halim, S. Kota, P. Urbankowski, B. Anasori, M. W. Barsoum, Y. Gogotsi, *ACS Appl. Mater. Interfaces* **2017**, *9*, 4296.
[30] Q. Yang, Z. Xu, B. Fang, T. Huang, S. Cai, H. Chen, Y. Liu, K. Gopalsamy, W. Gao, C. Gao, *J. Mater. Chem. A* **2017**, *5*, 22113.
[31] J. Zhang, N. Kong, S. Uzun, A. Levitt, S. Seyedin, P. A. Lynch, S. Qin, M. Han, W. Yang, J. Liu, X. Wang, Y. Gogotsi, J. M. Razal, *Adv. Mater.* **2020**, *32*, 2001093.
[32] N. Shpigel, A. Chakraborty, F. Malchik, G. Bergman, A. Nimkar, B. Gavriel, M. Turgeman, C. N. Hong, M. R. Lukatskaya, M. D. Levi, Y. Gogotsi, D. T. Major, D. Aurbach, *J. Am. Chem. Soc.* **2021**, *143*, 12552.
[33] B. Mendoza-Sánchez, Y. Gogotsi, *Adv. Mater.* **2016**, *28*, 6104.
[34] Y. Zhu, K. Rajouâ, S. Le Vot, O. Fontaine, P. Simon, F. Favier, *Nano Energy* **2020**, *73*, 104734.
[35] W. Liao, Y. Huang, H. Wang, H. Zhang, *Appl. Mater. Today* **2019**, *16*, 435.
[36] F. Ezzah Ab Latif, A. Numan, N. M. Mubarak, M. Khalid, E. C. Abdullah, N. A. Manaf, R. Walvekar, *Coord. Chem. Rev.* **2022**, *471*, 214755.
[37] E. Pomerantseva, Y. Gogotsi, *Nat. Energy* **2017**, *2*, 17089.
[38] M.-Q. Zhao, N. Trainor, C. E. Ren, M. Torelli, B. Anasori, Y. Gogotsi, *Adv. Mater. Technol.* **2019**, *4*, 1800639.
[39] D.-X. Song, L. Xie, Y.-F. Zhang, Y. Lu, M. An, W.-G. Ma, X. Zhang, *ACS Appl. Energy Mater.* **2020**, *3*, 7699.
[40] C. Tang, Y. Min, C. Chen, W. Xu, L. Xu, *Nano Lett.* **2019**, *19*, 5577.
[41] X. Xie, Z. Ao, D. Su, J. Zhang, G. Wang, *Adv. Funct. Mater.* **2015**, *25*, 1393.
[42] E. G. Da Silveira Firmiano, A. C. Rabelo, C. J. Dalmaschio, A. N. Pinheiro, E. C. Pereira, W. H. Schreiner, E. R. Leite, *Adv. Energy Mater.* **2014**, *4*, 1301380.
[43] J. Sun, H.-W. Lee, M. Pasta, H. Yuan, G. Zheng, Y. Sun, Y. Li, Y. Cui, *Nat. Nanotechnol.* **2015**, *10*, 980.
[44] Y. Zhang, H. Wang, Z. Luo, H. T. Tan, B. Li, S. Sun, Z. Li, Y. Zong, Z. J. Xu, Y. Yang, K. A. Khor, Q. Yan, *Adv. Energy Mater.* **2016**, *6*, 1600453.
[45] A. Rafieerad, A. Amiri, W. Yan, H. Eshghi, S. Dhingra, *Adv. Funct. Mater.* **2022**, *32*, 2108495.
[46] A. R. Hillman, *J. Solid State Electrochem.* **2011**, *15*, 1647.
[47] C. Weidlich, K.-M. Mangold, K. Jüttner, *Electrochim. Acta* **2005**, *50*, 1547.
[48] M. D. Levi, N. Levy, S. Sigalov, G. Salitra, D. Aurbach, J. Maier, *J. Am. Chem. Soc.* **2010**, *132*, 13220.
[49] W. Li, Z. Yang, M. Sun, J. Dong, *Rev. Phys.* **2022**, *9*, 100077.
[50] J. Rivera-Julio, A. González-García, R. González-Hernández, W. López-Pérez, F. M. Peeters, A. D. Hernández-Nieves, *J. Phys.: Condens. Matter* **2019**, *31*, 75301.
[51] M. S. Rathore, A. Vinod, R. Angalakurthi, A. P. Pathak, F. Singh, S. K. Thatikonda, S. R. Nelamarri, *Appl. Phys. A* **2017**, *123*, 708.
[52] T. P. Mernagh, L.-G. Liu, *Phys. Chem. Miner.* **1997**, *24*, 7.
[53] V. V. Atuchin, T. A. Gavrilova, S. A. Gromilov, V. G. Kostrovsky, L. D. Pokrovsky, I. B. Troitskaia, R. S. Vemuri, G. Carbajal-Franco, C. V. Ramana, *Cryst. Growth Des.* **2009**, *9*, 1829.
[54] V. Swamy, A. Kuznetsov, L. S. Dubrovinsky, R. A. Caruso, D. G. Shchukin, B. C. Muddle, *Phys. Rev. B* **2005**, *71*, 184302.

[55] X. Li, X. Yin, M. Han, C. Song, H. Xu, Z. Hou, L. Zhang, L. Cheng, *J. Mater. Chem. C* **2017**, *5*, 4068.
[56] M. Naguib, O. Mashtalir, M. R. Lukatskaya, B. Dyatkin, C. Zhang, V. Presser, Y. Gogotsi, M. W. Barsoum, *Chem. Commun.* **2014**, *50*, 7420.
[57] K. Ghosh, M. Pumera, *Small Methods* **2021**, *5*, 2100451.
[58] J. Vyskocil, C. C. Mayorga-Martinez, K. Szokölová, A. Dash, J. Gonzalez-Julian, Z. Sofer, M. Pumera, *ChemElectroChem* **2019**, *6*, 3982.
[59] H. Rokni, W. Lu, *Nat. Commun.* **2020**, *11*, 5607.
[60] K. Tang, W. Qi, Y. Wei, G. Ru, W. Liu, *Research* **2022**, *2022*, 9765121.
[61] J. Liu, T. Shen, J.-C. Ren, S. Li, W. Liu, *Appl. Surf. Sci.* **2023**, *608*, 155163.
[62] M. K. Aydinol, A. F. Kohan, G. Ceder, *J. Power Sources* **1997**, *68*, 664.
[63] J. A. Dawson, J. Robertson, *J. Phys. Chem. C* **2016**, *120*, 22910.
[64] R. A. Murugesan, K. C. Nagamuthu Raja, *Mater. Res. Bull.* **2023**, *163*, 112217.
[65] Q. T. Qu, B. Wang, L. C. Yang, Y. Shi, S. Tian, Y. P. Wu, *Electrochem. Commun.* **2008**, *10*, 1652.
[66] Q. Gao, W. Sun, P. Ilani-Kashkouli, A. Tselev, P. R. C. Kent, N. Kabengi, M. Naguib, M. Alhabeb, W.-Y. Tsai, A. P. Baddorf, J. Huang, S. Jesse, Y. Gogotsi, N. Balke, *Energy Environ. Sci.* **2020**, *13*, 2549.
[67] A. G. Volkov, S. Paula, D. W. Deamer, *Bioelectrochem. Bioenerg.* **1997**, *42*, 153.
[68] S. Koneshan, J. C. Rasaiah, R. M. Lynden-Bell, S. H. Lee, *J. Phys. Chem. B* **1998**, *102*, 4193.
[69] F. Razzaghi, C. Debiemme-Chouvy, F. Pillier, H. Perrot, O. Sel, *Phys. Chem. Chem. Phys.* **2015**, *17*, 14773.
[70] A. Vahidmohammadi, M. Mojtabavi, N. M. Caffrey, M. Wanunu, M. Beidaghi, *Adv. Mater.* **2019**, *31*, 1806931.
[71] J. Kankare, *Langmuir* **2002**, *18*, 7092.
[72] N. Shpigel, M. D. Levi, S. Sigalov, T. S. Mathis, Y. Gogotsi, D. Aurbach, *J. Am. Chem. Soc.* **2018**, *140*, 8910.
[73] Y. Zhang, Y. Liang, H. Dong, X. Wang, Y. Yao, *J. Electrochem. Soc.* **2020**, *167*, 070558.
[74] P. E. Blöchl, *Phys. Rev. B* **1994**, *50*, 17953.
[75] G. Kresse, D. Joubert, *Phys. Rev. B* **1999**, *59*, 1758.
[76] J. Klimes, D. R. Bowler, A. Michaelides, *Phys. Rev. B* **2011**, *83*, 195131.
[77] A. Lozano, B. Escribano, E. Akhmatskaya, J. Carrasco, *Phys. Chem. Chem. Phys.* **2017**, *19*, 10133.